CCFE
CULHAM CENTRE FOR FUSION ENERGY

UK Atomic Energy Authority

UKAEA-CCFE-PR(25)327

Bochuan Sun, Mark Fedorov, Jan Wrobel, Duc Nguyen-Manh, Caleb Hatler, Matthew Vigil, Dan J. Thoma, Osman El-Atwani, Enrique Martinez

Thermodynamic Assessment of the Quaternary WTaCrV Refractory High Entropy Alloy as a Means to Guide Experimental Approaches

Thermodynamic Assessment of the Quaternary WTaCrV Refractory High Entropy Alloy as a Means to Guide Experimental Approaches

Bochuan Sun, Mark Fedorov, Jan Wrobel, Duc Nguyen-Manh, Caleb Hatler, Matthew Vigil, Dan J. Thoma, Osman El-Atwani, Enrique Martinez

This is a preprint of a paper submitted for publication in Acta Materialia

Thermodynamic Assessment of the Quaternary WTaCrV Refractory High Entropy Alloy as a Means to Guide Experimental Approaches

Bochuan Sun[1], Mark Fedorov[2], Jan Wrobel[2], Duc Nguyen-Manh[3], Caleb Hatler[4], Matthew Vigil[4], Dan J. Thoma[4], Osman El-Atwani[5], Enrique Martinez[1,6,]*

[1]Department of Materials Science and Engineering, Clemson University, Clemson, SC, 29634, USA

[2]Faculty of Materials Science and Engineering, Warsaw University of Technology, ul. Wołoska 141, 02-507, Warsaw, Poland

[3]Materials Division, United Kingdom Atomic Energy Authority, Abingdon, OX14 3DB, United Kingdom

[4]Department of Materials Science and Engineering, University of Wisconsin-Madison, Madison, WI, 53706, USA

[5]Reactor Materials Group, Nuclear Sciences Division, Pacific Northwest National Laboratory, Richland WA, 99352, USA

[6]School of Mechanical and Automotive Engineering, Clemson University, Clemson, SC, 29634, USA

Abstract

High-entropy alloys (HEAs) are being explored as potential candidates for radiation-tolerant materials, with some compositions exhibiting good resistance to defect cluster formation. One such system is WTaCrV, although only a single composition has been experimentally tested under ion irradiation, where it showed phase decomposition at low temperature. In this work, we systematically investigate the thermodynamic properties of the entire quaternary composition space. Using a combination of first-principles calculations, cluster expansion, and Monte Carlo simulations, we access temperature-dependent free energy functionals, short-range ordering parameters, and atomic configurations that can be compared with experimental observations. These data are then used to construct the phase stability map and thermodynamic databases (TDBs) that illustrate BCC phase stability across the composition space. Our results identify compositional regions that are less likely to undergo phase separation at low temperatures. These insights provide predictive guidance for selecting compositions that are more likely to remain single-phase solid solutions, which we have validated with experimental results.

1. Introduction

Tungsten (W) is one of the most favorable materials for plasma-facing components and divertors in fusion devices due to its high melting temperature and low tritium retention [1,2,3]. Unfortunately, W has also a low fracture toughness, which complicates its manufacturing. Furthermore, after irradiation and implantation with helium (He) and deuterium, dislocation loops, He bubbles, craters, and holes have been frequently observed [4,5,6,7]. To overcome these drawbacks, high entropy alloys (HEA)

have drawn particular attention because of their significant potential to reduce irradiation effects [8,9,10,11], which enables the combination of the advantages of various metal elements while mitigating their respective shortcomings.

There have been many attempts to develop different HEAs and each facing challenges. In TaTiWVCr HEA, recrystallization occurred after exposure to 5×10^{16} ions/cm² in the HEA film at 1073 K. The HEA film also exhibited He bubbles and dislocation loops under He^{+} irradiation at a flux of 5.56×10^{13} cm^{-2} s^{-1} and fluences ranging from 1×10^{16} cm^{-2} to 2×10^{17} cm^{-2} [12]. A high density of dislocation loops was also observed in CoCrMnFeNi and $Al_{0.3}$CoCrFeNi HEAs [13]. The increase in irradiation hardness for these two compositions significantly surpasses that of alloy SS316H irradiation damage up to 1.3 dpa under 1 MeV Kr ion with a flux of 6.3×10^{15} ions/(m^2·s) at both 300 K and 500 K [13, 14], and irradiation-induced segregation is observed in CoCrFeMnNi when irradiated at 673 K [15]. Furthermore, irradiation-induced voids and dislocation loops cause significant swelling in $Fe_{38}Mn_{40}Ni_{11}Al_4Cr_7$, AlxCoCrFeNi and HfNbTaTiZr HEAs [16, 17, 18]. Contrarily, CoCrFeMnNi HEA has a good resistance to swelling, although Co can absorb neutrons and transmute into ^{60}Co, limiting its application as plasma facing component [19, 20]. Cr can modify the diffusivity of vacancies to accelerate the formation of voids and dislocation loops, especially in FCC alloys, such as, FeNiCr [21] and CrFeNiMn [22]. Due to its high neutron capture cross-section [23], Ni typically acts as a transmutation center [24, 25] and poses radioactivity issues in fusion environments. When adding Nb to W, and manufacturing using a laser powder-bed-fusion method, cracks are often observed from W-5Nb binary alloys to MoNbTaW HEAs [26, 27, 28], with Nb also bearing radioactive concerns. BCC crystalline structures generally have higher stacking fault energy and lower atomic packing fraction, leading to greater irradiation tolerance compared to FCC structures. However, phase instability remains a significant challenge, as defects tend to accumulate at the interface between precipitate phases and the matrix, which might increase irradiation hardening and embrittlement [29]. Furthermore, HEAs have many potential applications due to their excellent corrosion resistance, biocompatibility, and wear resistance [30, 31, 32].

In 2019, a study on $W_{38}Ta_{36}Cr_{15}V_{11}$ HEA with a body-center cubic (BCC) lattice structure indicated that after exposure to ion irradiation, no loops were observed even at a high dose (8 dpa) [33]. Compared to other potential materials (such as WTiC, nanocrystalline W, etc.), this HEA has a higher resistance to He bubble formation [34]. However, the main drawback of this composition is that the order-disorder transition temperature (ODTT) is high (~1,400 K), which indicates the system phase decomposes below 1,400 K. Below this temperature, WTa and VCr rich phases appear, first as solid solutions and then further transform to intermetallics as the temperature decreases further. This phase decomposition may modify the material properties in operandum, which might result in uncontrolled responses. Hence, it is necessary to understand the thermodynamic driving forces leading to such microstructural changes and how they vary as a function of composition. Identifying compositions with lower ODTTs and comparable irradiation resistance can allow for the optimization of the material.

In this work, we explore the whole composition range of BCC WTaCrV HEAs [33], study the thermodynamic properties of each composition, calculate the Warren-Cowley short-ranged order (SRO) parameters [35, 36] and the ODTT. The modeling results inform experimental approaches on optimal compositions. We observe that experimental results follow the trend obtained from the modeling methodology. Moreover, we created a thermodynamic database at different temperatures, and couple with a Calculation of Phase Diagrams (CALPHAD) approach as implemented in OpenCALPHAD [37, 38] to draw a quaternary phase diagram.

2. Methodology

The cluster expansion (CE) formalism is a tool for studying HEAs due to its exceptional ability to reveal the effects of different alloy compositions on the overall thermodynamic properties [39, 40, 41]. Fitting the CE models requires the mixing energy of different atomic configurations, which can be accurately determined using density functional theory (DFT). The Metropolis Monte Carlo (MC) method [42, 43] is used to obtain equilibrium states for different temperatures. We have used the Alloy Theoretic Automated Toolkit (ATAT) code [44, 45] to fit the CE and to perform the MC simulations. The enthalpy of mixing of a K-component alloy is defined as:

$$\Delta H_{mix}^{DFT} = E_{tot} - \sum_{p=1}^{K} C_p E_p \,, \tag{3}$$

where E_{tot} is the total energy per atom of the alloy, C_p is the average concentration of the p component, and E_p is the cohesive energy of the pure element in the BCC crystal structure. The cluster expansion predicts ΔH_{mix} as [39, 46, 47, 48, 49, 50]:

$$\Delta H_{mix}^{CE}(\vec{\imath}) = \sum_{\omega} m_\omega J_\omega < \Gamma_\omega(\vec{\imath}) >_\omega \,, \tag{4}$$

where $\vec{\imath}$ is the configurational occupation vector, ω is the cluster number, m is the multiplicity factor that indicates the number of clusters that are equivalent by symmetry (divided by the number of lattice sites), J is the concentration-independent effective cluster interactions (ECI), that we fit to DFT results applying the structure inversion method, and $< \Gamma_\omega(\vec{\imath}) >_\omega$ are the average correlation functions that can be calculated as [51]:

$$\Gamma_\omega^{(s)}(\vec{\imath}) = \gamma_{j_1,K}(i_1)\gamma_{j_2,K}(i_2)\gamma_{j_3,K}(i_3)\cdots\gamma_{j_\omega,K}(i_\omega) \tag{5}$$

where $\gamma_{j,K}(i)$ are point functions denoting the occupancy of each cluster, (s) = $\{j_1, j_2, \ldots, j_\omega\}$ is the decoration of the cluster by point functions. The point functions need to be orthogonal, and for a K-component system [44] we can use:

$$\gamma_{j,K}(i) = \begin{cases} 1 & if\ j = 0, \\ -\cos\left[2\pi\left(\frac{j}{2}\right)\frac{i}{K}\right] & if\ j > 0\ and\ odd, \\ -\sin\left[2\pi\left(\frac{j}{2}\right)\frac{i}{K}\right] & if\ j > 0\ and\ even, \end{cases} \quad (6)$$

To validate the fitting, the cross-validation (CV) score is used to indicate the accuracy [44, 45]:

$$\mathrm{CV} = \sqrt{\frac{1}{N}\sum_{i=1}^{N}\left(\Delta H_{mix}^{DFT}(\vec{\imath}) - \Delta H_{mix}^{CE}(\vec{\imath})\right)^2}\ , \quad (7)$$

which is calculated from the mean squared error between the DFT energies and the CE predicted energies and N is the total number of structures used to fit the ECIs. The CE model was developed and calibrated by Alvarado et al. [52] for the CrHfTaVW quinary HEA. Here, we calculated various thermodynamic properties for quaternary CrTaVW compositions with 10 at% step increments in concentration, including the equiatomic composition. We also computed thermodynamic functions for binary and ternary compositions, with step increments of 20 at%. The MC method is performed to determine the equilibrium state at different temperatures in the range of 0 to 2000 K with increments of 10 K. Most compositions reach fully a random state at 2000 K and hence the ODTT of all systems are below 2000 K. The simulation cell was 16x16x16 cubic unit cells in each dimension, containing 8192 atoms. The thermodynamic integration (TDI) scheme as developed in Refs. [38, 42, 53] is used to calculate the configurational entropy of mixing:

$$S_{mix}(T) = \int_0^T \frac{C_V(T')}{T'} dT' \quad (8)$$

where the specific heat $C_V(T)$ is obtained from the fluctuations in the energy [42]:

$$C_V(T) = \frac{\langle H_{mix}(T)^2\rangle - \langle H_{mix}(T)\rangle^2}{T^2}. \quad (9)$$

Then, the free energy of mixing can be calculated as [42]:

$$G_{mix} = H_{mix} - TS_{mix}, \quad (10)$$

3. Results

3.1 Validation

The CE used in this work was thoroughly validated in Ref [52], mainly against enthalpies of mixing at 0 K obtained from DFT as part of the testing but also against experiments, showing remarkable agreement. This cluster expansion model includes 60 binary, 80 ternary, and 55 quaternary clusters, and achieves a cross-validation (CV) score of 0.0133, which is better than other cluster selections. For

instance, a model with 50 binary, 80 ternary, and 55 quaternary clusters has a CV score of 0.0145, while another with 60 binary, 120 ternary, and 55 quaternary clusters results in a CV score of 0.0150. To further validate our approach, we compare thermodynamic properties with previous models available in the literature. The thermodynamic properties versus temperature of the equiatomic CrTaVW alloy is shown in Figure 1, with Figs.1(a) and 1(b) presenting the results from the current model and the same composition from Ref [53], which were obtained following a similar CE approach for the quinary CrTaTiVW system. To improve visual comparison, we rename the S_{mix} as S_{conf} and the ideal configurational entropy of mixing S_{ideal} as S_{rand} specifically in this figure. The shape and value of the enthalpy of mixing curve shows a good agreement between these two CE models. The only difference is that at 3000 K, the system in our calculation reaches a fully random state, with the configurational entropy of mixing closely approaching the ideal configurational entropy of mixing. This is due to the improved accuracy of the CE model [52] we use in this work, which includes additional 4-body cluster interaction, with respect to the model in Ref [53]. The peaks shown near 200 K highlighted in the black dashed box are due to the transition of the TaW pair from a solid solution phase to an ordered compound.

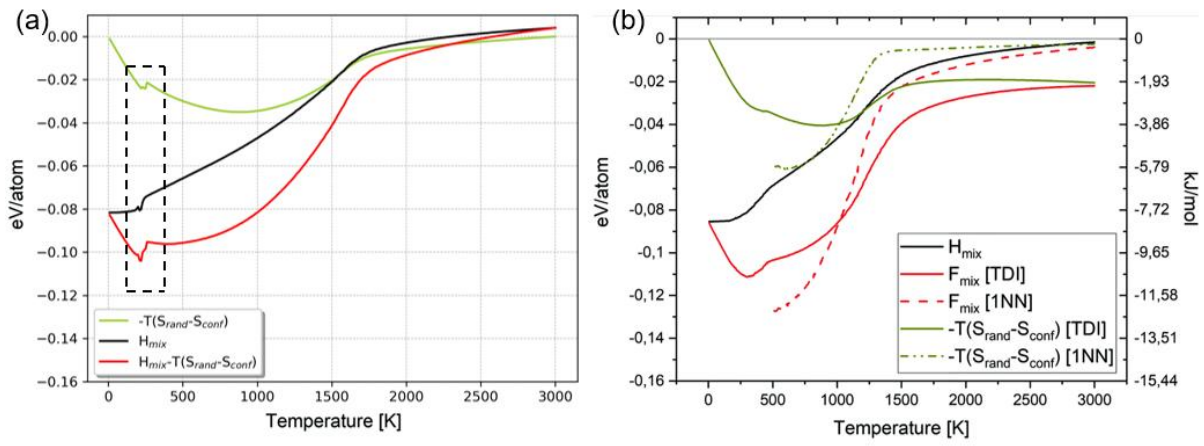

Figure 1. (a) The thermodynamic properties of the equiatomic CrTaVW high entropy alloy obtained with the current model. (b) The thermodynamic properties of the same composition in Sobieraj's el al. study [53].

3.2 Thermodynamic Properties

To investigate the phase stability across various compositions of the WTaCrV system, their thermodynamic properties were calculated, encompassing the enthalpy of mixing (H_{mix}) , configurational entropy of mixing (S_{mix}), and free energy of mixing (G_{mix}), employing CE-based Monte Carlo simulations. This approach enables a detailed understanding of the energetics and configurational behaviors of HEAs, providing insights into their structural stability.

In Fig. 2, we plot the H_{mix}, $-TS_{mix}$, and G_{mix} per atom at 1000 K (Fig. 2(a)) and 2000 K (Fig. 2(b)). H_{mix} is obtained from the MC simulations, S_{mix} is calculated relying on TDI, and G_{mix} is the sum

of H_{mix} and $-TS_{mix}$. To illustrate the dependence of the thermodynamic potentials on composition, a tetrahedral plot is the most suitable representation. In this type of plot, each vertex corresponds to a pure element, providing a clear view of the compositional relationships and interactions between elements in a multicomponent system. Each tetrahedral plot contains 133 different compositions. By comparing the results at different temperatures, we observe that $-TS_{mix}$ dominates the G_{mix} at higher temperatures, reflecting the high-entropy effect typical of high-entropy alloys. Additionally, the H_{mix} is overall positive, which indicates that the system has a tendency toward phase decomposition.

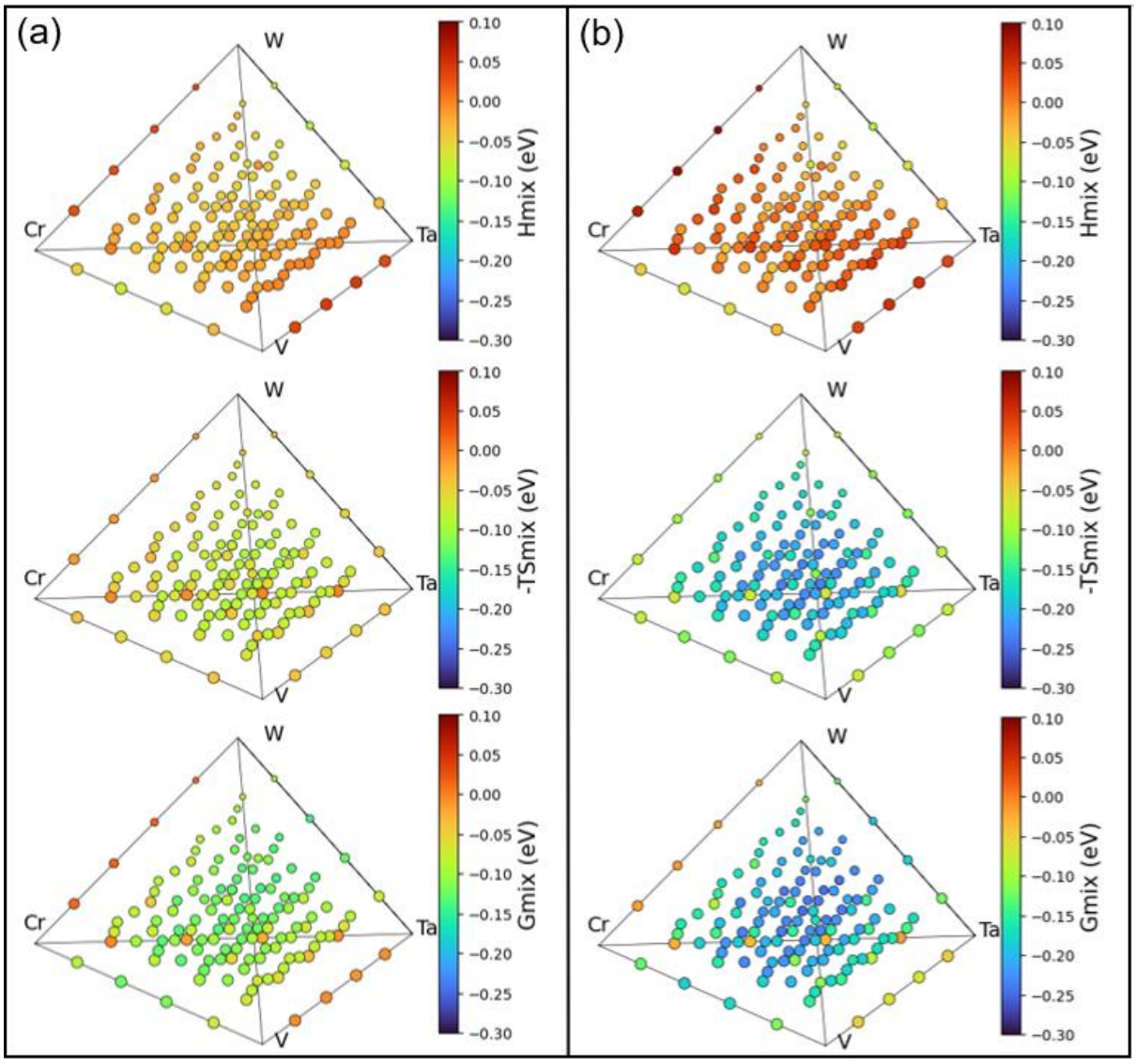

Figure 2. H_{mix}, $-TS_{mix}$, and G_{mix} per atom of different compositions and temperatures (a) 1000 K and (b) 2000 K.

To enhance visual clarity, the size of the circles in the figures is inversely correlated with the W atomic fraction; specifically, smaller and larger points indicate higher and lower W content, respectively. Figure 3 shows the values in a 2D cross section of the tetrahedron for G_{mix} at 20 at% Cr and another one at 20 at% Ta. The local minimum on the free energy landscape at 2000 K is deeper compared with the

same composition at 1000 K, which highlights the role of entropy on the alloy stability.

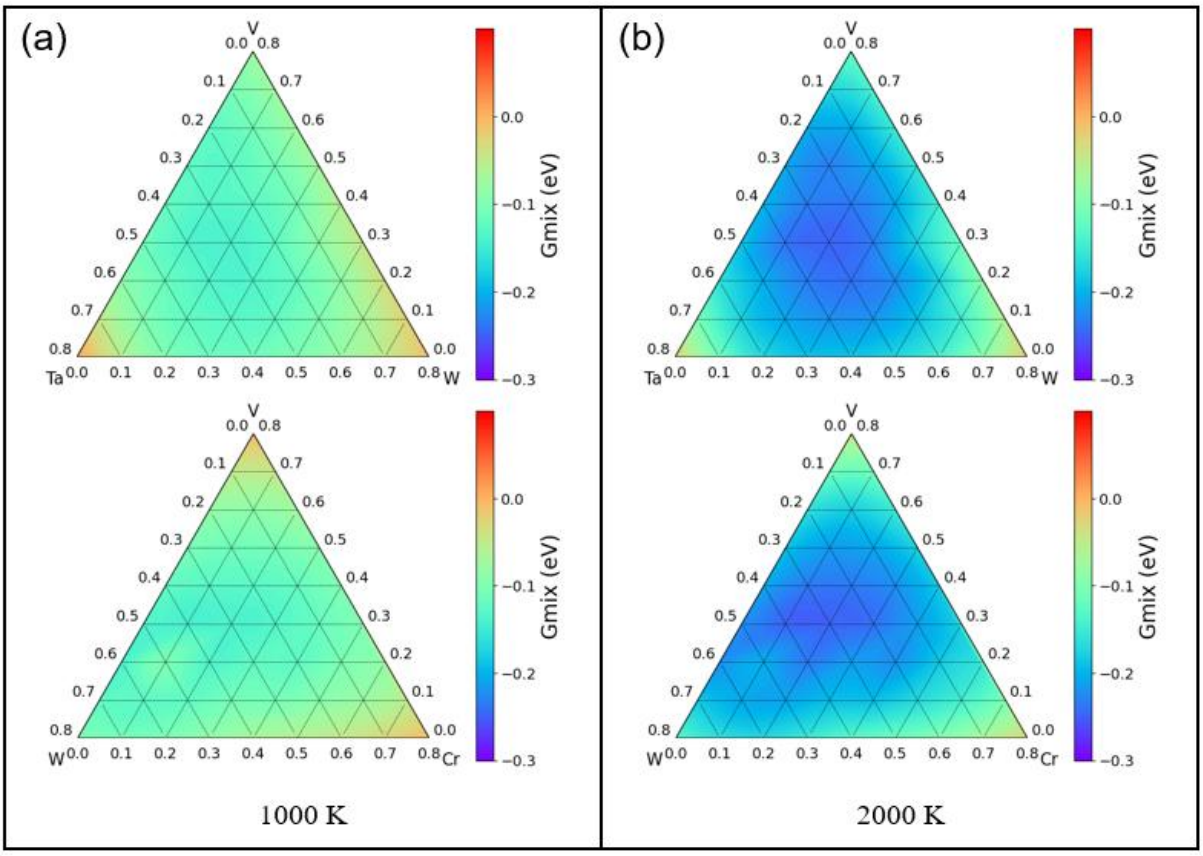

Figure 3. G_{mix} per atom of different compositions with 20% Cr (top) and 20% Ta (bottom). (a) at 1000 K, and (b) at 2000 K.

3.3 Short-Range Order Parameters and Order-disorder transition temperature

As temperature increases, the system undergoes a transition from ordered/segregated phases to a single solid solution phase. To quantitatively characterize this transition, the Warren-Cowley short-range order (SRO) parameter and the order-disorder transition temperature (ODTT) are introduced.

The Warren-Cowley SRO parameter of atom types *i* and *j* can be calculated from pair probabilities [35, 36]:

$$\alpha_n^{ij} = 1 - \frac{y_n^{ij}}{c_i c_j}. \tag{11}$$

In this equation, *n* denotes the n-th nearest neighbor, and y_n^{ij} is the probability to find the specific *i-j* pair in the n-th neighboring shell, which can be obtained by a matrix inversion of the correlation functions obtained from the CE, and c_i, c_j are the global concentration of atom types *i* and *j*.

In this study, we consider first and second nearest neighbors as well as average (α_{avg}) SRO parameters

in a BCC crystalline structure calculated as [54]:

$$\alpha_{avg} = \frac{8\alpha_1 + 6\alpha_2}{14}, \tag{12}$$

A positive SRO parameter indicates a repulsive relationship between two different elements, while a negative SRO parameter indicates an attractive interaction. When the SRO parameter is zero the system is in a random solid solution phase. In Fig. 4, we present the average SRO parameters as a function of temperature on the left panels and example atomic configurations on the right, plotted with the open visualization tool (OVITO) [55] for $Cr_{0.1}Ta_{0.1}V_{0.7}W_{0.1}$ (Fig. 4(a)) and an equiatomic composition (Fig. 4(b)) at 1000 K and 2000 K. SRO plots show similar trends, the system phase separates in domains rich in CrV and WTa at low temperatures while at high temperatures the value approaches 0 (fully random configurations). Moreover, the fact that the SRO is negative for these pairs of atom types indicates that Cr and V tend to order as do W and Ta. The rest of the pairs show positive SRO values implying a repulsive interaction between them, that is, Cr and V repel W and Ta and hence the microstructure shows the compositional regions mentioned above. For the composition rich in V (Fig. 4(a)), the SRO becomes close to 0 at about 900 K, i.e., at that temperature the system becomes a solid solution, while for the equiatomic composition, the SRO reaches 0 at around 1700 K. This difference can be clearly seen in the atomic configurations shown in the figure where domains rich in CrV and WTa are distinguished for the equiatomic compositions. At 1000 K, the equiatomic alloy still presents regions rich in WTa and CrV, while the V rich system looks random. On the other hand, at 2000 K both compositions show a random distribution of atom types in agreement with the SRO plots. These kinds of phase decomposition can be compared to atom probe tomography results, as it has been done previously [33, 52, 56], to validate the results.

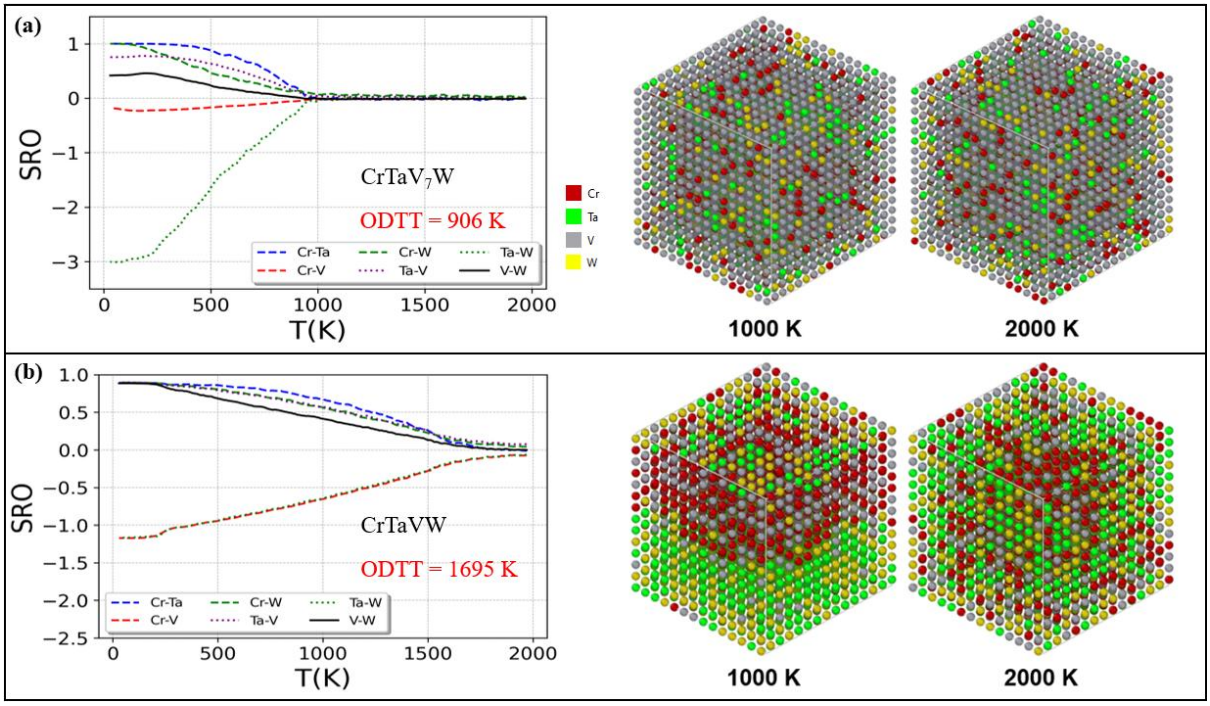

Figure 4. SRO parameters as a function of temperature and atomic configurations at 1000 K and 2000 K of different compositions, (a) $Cr_{0.1}Ta_{0.1}V_{0.7}W_{0.1}$, (b) equiatomic CrTaVW composition.

Since the ODTT is composition dependent, to more easily capture the influence of compositional variations on this parameter, we present a tetrahedral plot in Fig. 5(a) that encompasses more than 80 quaternary compositions, alongside 24 ternary and 24 binary alloys.

The calculation of the ODTT primarily relies on identifying the inflection point on the ΔH_{mix} versus temperature curve, that allows for the identification of both first- and second-order phase transitions. However, for certain compositions, we also consider situations where the absolute values of the SRO parameters are sufficiently small, as described above. For both binary and ternary and alloys, the concentration increments are set to 20 at%, while it is 10 at% for the quaternaries, and the size of the circles in Fig. 5(a) is anti-correlated with W content, as above. In Figs. 5 (b)-(e), we show cuts of the tetrahedral figure (Fig. 5(a)) with Cr 20 at%, Ta 20 at%, V 20 at% and W 20 at% planes, respectively, and draw the ODTT landscape in the cross section.

This representation enables an immediate grasp of the diversity of alloy compositions explored in this study. Notably, in both ternary and quaternary HEAs, a high concentration of V is generally associated with lower ODTTs, indicating enhanced solid solution stability, whereas a high concentration of Cr leads to higher ODTTs, suggesting an increased tendency toward phase decomposition at elevated temperatures. These trends provide a useful guidance for the future experimental design of materials.

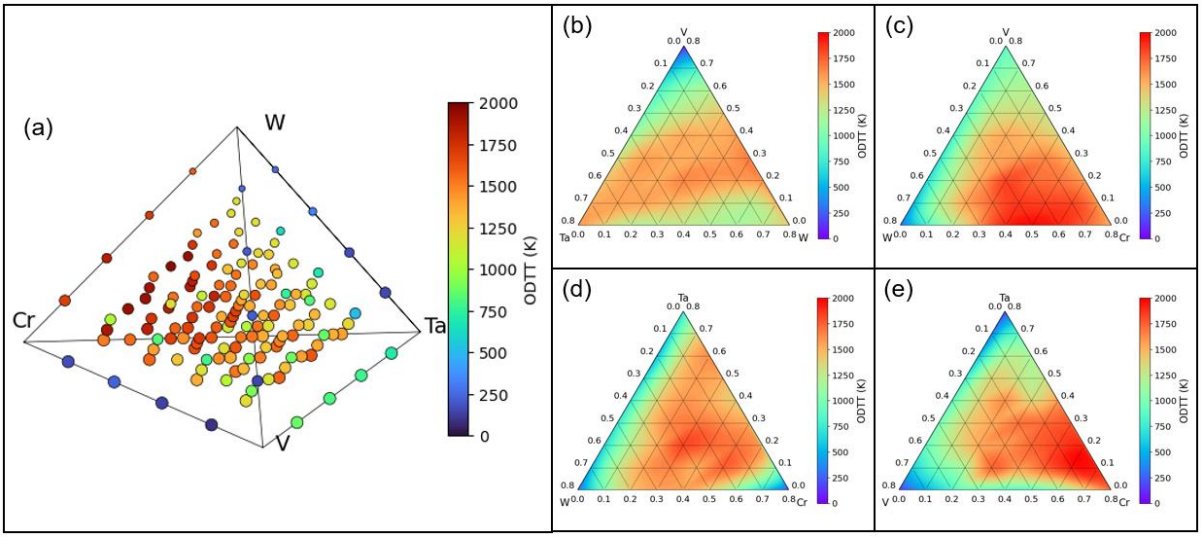

Figure 5. (a) ODTT tetrahedral plot for different compositions. b), c), d) and e) show cuts at Cr 20 at%, Ta 20 at%, V 20 at% and W 20 at% planes, respectively, with ODTT interpolated values in 2D maps.

3.4 Phase stability map of different BCC structures

From the free energy dependence on composition and temperature for all compositions studied, we have generated a thermodynamic database file (TDB), which can be used in computational thermodynamics codes to compute the phases at equilibrium. In this study the only crystallographic structure that was

considered is BCC, and hence the goal is to understand in what compositional regions the system decomposes in different BCC phases. We used OpenCALPHAD [37] to calculate the common tangent on a four-dimensional compositional space. The TDB file includes the Gibbs free energy of each composition [37, 38],

$$G_{tot} = G_{ref} + G_{ideal} + G_{xs}\,. \tag{13}$$

G_{ref} is the reference energy of the pure elements present in the alloy, in this study we used the energy from first principles, G_{ideal} is the contribution from the ideal entropy of mixing [61], equal to $-TS_{ideal}$,

$$S_{ideal} = -k_B \sum_{i=1}^{K} x_i \ln x_i \tag{14}$$

where k_B is the Boltzmann constant, K is the total number of elements, and x_i is the atomic fraction of the ith element. In this study, to have a more precise configurational entropy, we use the TDI results from MC simulations instead of the ideal configurational entropy.

G_{xs} is the excess Gibbs free energy, which includes the non-ideal interactions between different elements. We obtain G_{xs} from our MC simulations for each composition and temperature [37]:

$$G_{xs}^{MC} = H_{mix} - G_{ref} - T(S_{mix} - S_{ideal}) \tag{15}$$

We employed the sqs2tdb fitting command in ATAT [57] to calculate the excess Gibbs free energy as a sum of different polynomials. In this study, the fitting result for the quaternary polynomial contributions $L_{A,B,C,D}$ equals to 0, hence we only have the binary and ternary contributions as shown in equations (16) and (17) [57].

$$G_{xs}^{binary} = x_A x_B \sum_{v=0}^{n} L_{A,B}(x_A - x_B)^v\,, \tag{16}$$

$$G_{xs}^{Ternary} = L_{A,B,C} x_A x_B x_c (V_A x_A + V_B x_B + V_C x_C). \tag{17}$$

v is the level of the polynomial expansion, and we have used levels from 1 to 3 to analyze its effect on the accuracy of the fitting. x_i is the concentration of element i, and $V_i = x_i + (1 - x_A - x_B - x_C)/3$. sqs2tdb fits the L parameters to the excess free energies and stores the values in a TDB file.

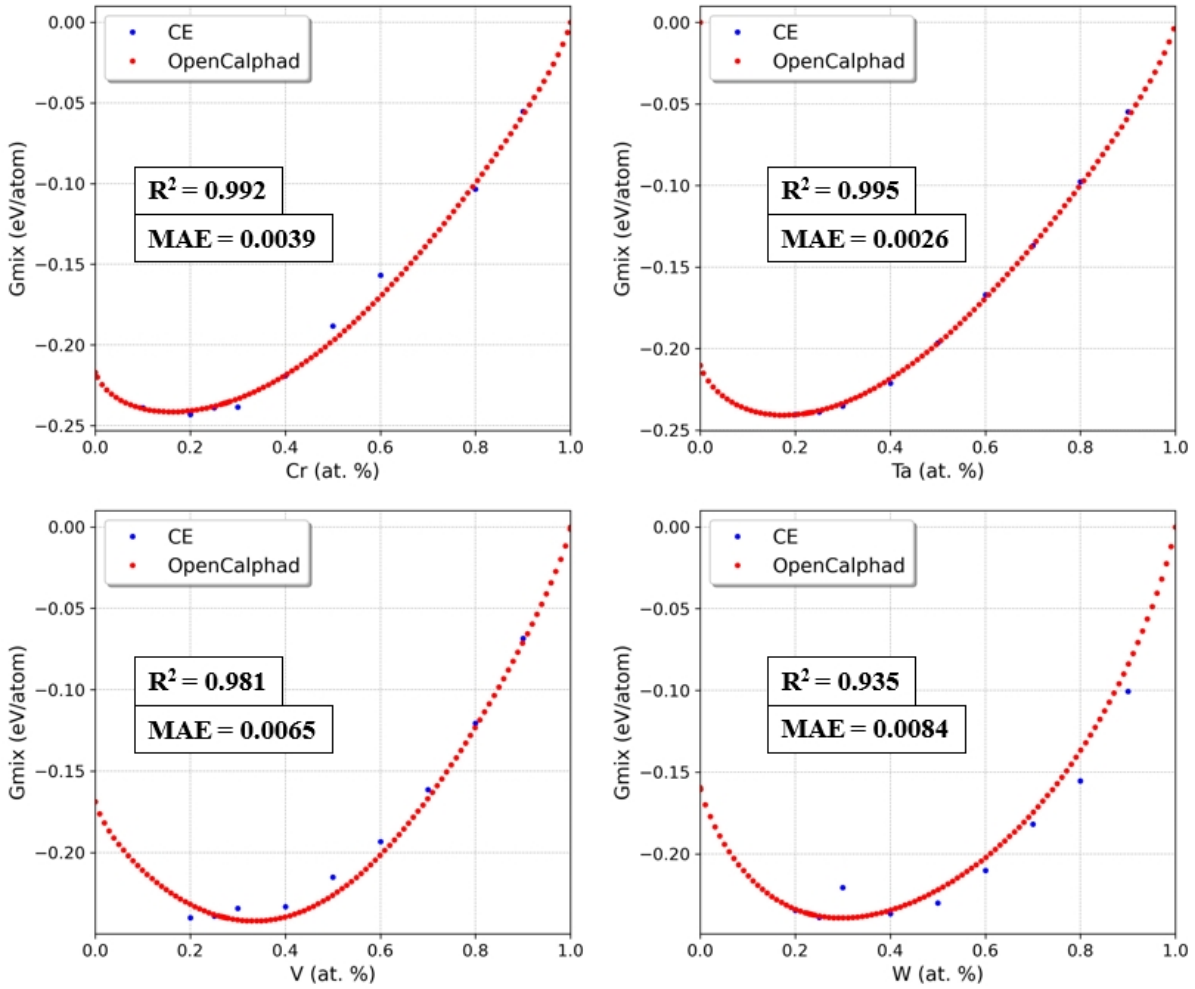

Figure 6. G_{mix} of different pseudo-binary compositions calculated from cluster expansion and CALPHAD method with different levels of binary polynomials on excess G_{mix} at 2000 K

To validate our calculation on the phase stability map, we compute the G_{mix} from cluster expansion and the CALPHAD approach for different pseudo-binary compositions, $\mathrm{Cr}_x(\mathrm{TaVW})_{1-x}$, $\mathrm{Ta}_x(\mathrm{CrVW})_{1-x}$, $\mathrm{V}_x(\mathrm{CrTaW})_{1-x}$, and $\mathrm{W}_x(\mathrm{CrTaV})_{1-x}$, with an increment of 10 at%. The results are shown in Fig. 6, and it should be noted that, for those CE data points, only $\mathrm{A}_{0.7}(\mathrm{BCD})_{0.1}$, $\mathrm{A}_{0.4}(\mathrm{BCD})_{0.2}$, $\mathrm{A}_{0.1}(\mathrm{BCD})_{0.3}$ and equiatomic compositions are used to fit the L coefficients and generate the TDB files. The difference between the CE and CALPHAD methods is small enough to consider the simulation results reliable, with the coefficient of determination (R^2) and mean absolute error (MAE) between OpenCALPHAD and CE shown in the figure.

With the choice of level 3 polynomials for binary terms, we calculated the phase stability map at 2000 K shown in Fig. 7, where the number of phases for each composition is shown as obtained from OpenCALPHAD and the generated TDB database. The total number of compositions in the tetrahedral plot is 1771, with concentration increments set at 5 at% to explore a larger composition space without running the comparably expensive Monte Carlo simulations. While this diagram does not represent a

full equilibrium phase diagram accounting for all possible crystal structures, it provides thermodynamically meaningful phase stability information constrained within the BCC lattice framework.

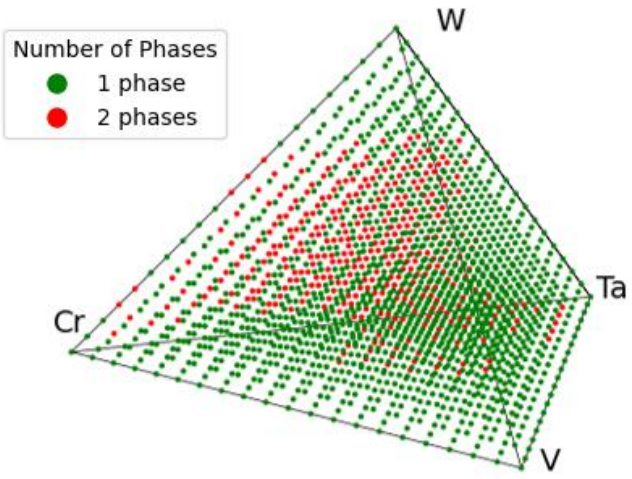

Figure 7. One- and two-phase regions at 2000 K in the quaternary WTaCrV phase stability map.

In compositions with two phases, we mainly see a phase rich in W and Ta and another one rich in Cr and V, including for the equatomic composition (phase 1 with a fraction of 0.805: 21%at W, 20%at Ta, 30%at Cr, 29%at V; phase 2 with a fraction of 0.195: 41%at W, 45%at Ta, 7%at Cr, 7%at V) and the $W_{38}Ta_{36}Cr_{15}V_{11}$ (phase 1 with a fraction of 0.28: 20%at W, 16%at Ta, 37%at Cr, 27%at V; phase 2 with a fraction of 0.72: 45%at W, 44 %at Ta, 6%at Cr, 5%at V), tested experimentally observing similar phase decomposition of rich Cr-V and rich W-Ta.

4. Discussion

4.1 Experimental Design

Precipitation hardening is commonly observed in HEAs, where finer lamellae, and/or small particles, act as obstacles to dislocation motion, enhancing strength but often resulting in reduced ductility [58, 59, 60]. Therefore, studying the order-disorder transition is a viable approach for guiding future manufacturing, such as deciding composition, annealing temperature, or heating and cooling rates. The crystal structure of the phases and their composition also affect the mechanical properties as dislocations interact with precipitates and hinder dislocation glide. Our simulations offer insights that can guide experiments in determining optimal compositions. Based on the desired hardness and ductility, they can select the most favorable composition by using the predictions of the ODTT and the atomic fraction of intermetallic phases. Also, after synthesis and measurement, once we obtain the specific composition, we can validate the theoretical model comparing to experimental results, as it has been done with atomic structures as obtained with CE-MC and atom probe tomography [33].

4.2 Experimental observations

To experimentally validate the ODTT approach as a design parameter, three samples were compared

with a broad range of ODTT values. Three WTaVCr ingots were arc cast in an ultra-high purity argon (99.999%) environment. Elemental W, Ta, and Cr (99.95%) and V (99.9%) were melted together on a water-cooled copper crucible. To prepare the environment for arc melting, the chamber was evacuated with a roughing pump to $2x10^{-3}$ torr and back-filled with Ar three times to reduce the partial pressure of oxygen and nitrogen. A titanium getter button was melted before the WTaVCr to reduce residue levels of oxygen and nitrogen. The ingots were 10-15 grams and were melted four times.

The samples were heat-treated at 1400 ºC for 24 hours in slight positive pressure, ultra-high purity Ar flowing environment. The samples were wrapped in Ta foil (99.95%) and placed in an alumina boat. The tube furnace was evacuated and purged similar to the arc-casting process, and the samples were furnace cooled.

Samples were cross-sectioned into minimum ~3 mm thick wafers and mounted in conductive filled phenolic mounting compound using a hot-press. Samples were then ground flat using 320 to 600 grit silicon carbide polishing paper and polished with 9 µm, 3 µm and 1 µm diamond suspensions and finished using vibratory polishing with 0.05 µm colloidal silica suspension.

After polishing, samples were imaged on the Hitachi S3400N SEM with BSE. EDS was done using an Oxford Instruments X-act with AZtec spectrum analysis. EDS detection was done at 20 kV at a ~10 mm working distance with ~25-40% deadtime and sum peaks removed. EDS was done over a ~260x195 μm^2 area, where W, and Ta were measured using the L-α characteristic peak, and Cr and V were measured using the K-α characteristic peak. It should be noted that there is an overlap in the V K-β (5.428 KeV) and Cr K-α (5.415 KeV), so the measured values of Cr may have a wider margin of error. The measured compositions of each sample are listed in table 1.

Predicted ODTT	Measured composition (at %)			
	W	Ta	Cr	V
489 K	46.9	43.5	0.4	9.2
1408 K	10.1	38.4	14.6	36.9
1628 K	18.7	24.2	33.8	23.3

Table 1. Composition and ODTT of 3 samples

Finally, X-ray Diffraction (XRD) patterns were obtained using Cu Ka radiation at 50 KeV and 1000 µA. The Bruker D8 Discovery X-ray diffractometer was operated with 2θ angles from 20º to 100º at 10º increments and 60 s dwell times.

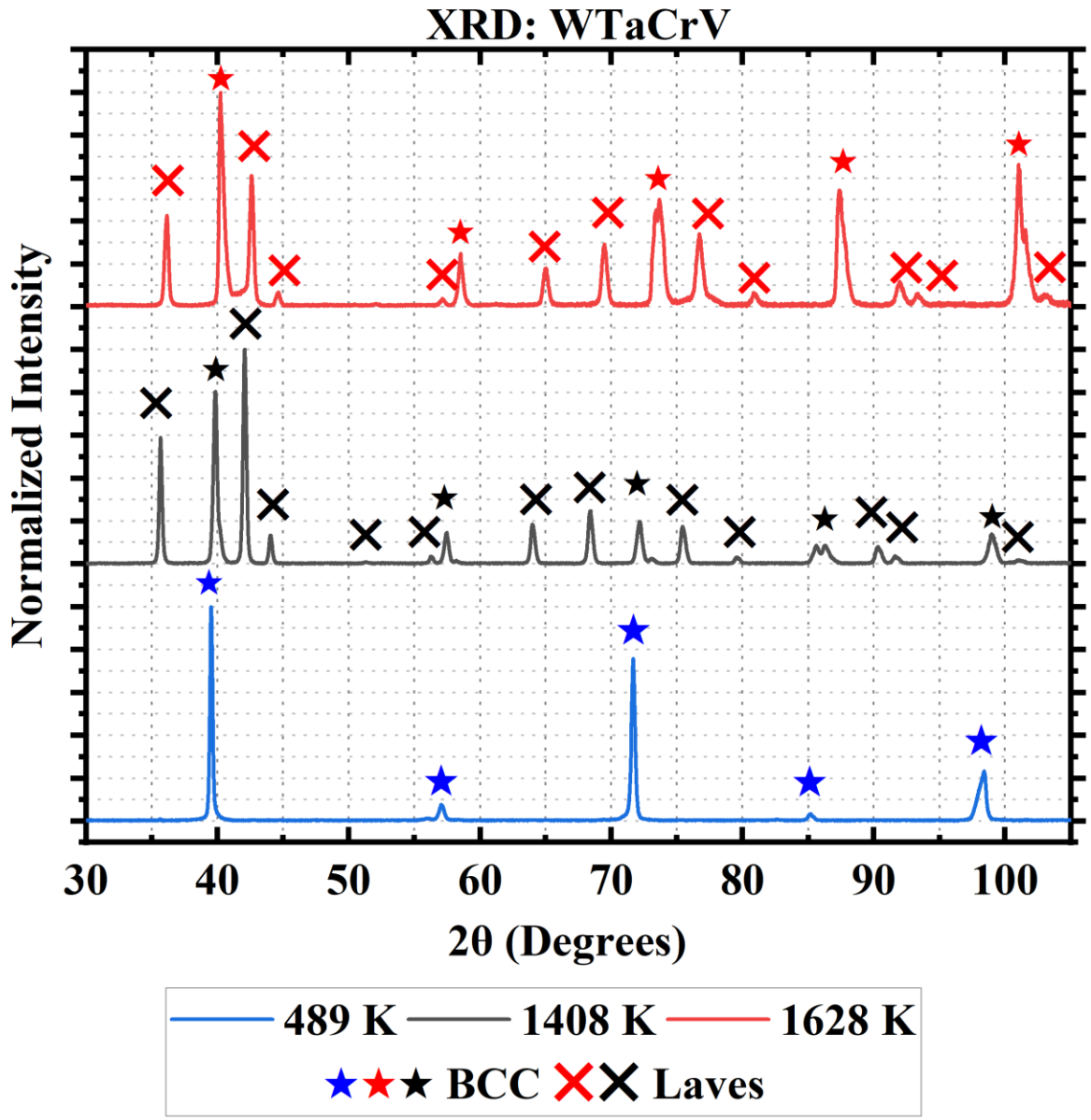

Figure 8. XRD patterns of arc cast and heat-treated samples from highest to lowest ODTTs. The higher ODTT samples (1628 K: $W_{19}Ta_{24}Cr_{34}V_{23,}$ 1408 K: $W_{10}Ta_{38}Cr_{15}V_{37}$) exhibit a large volume fraction of an ordered intermetallic Laves phase, while the lower calculated ODTT sample (489 K: $W_{47}Ta_{43.5}Cr_{0.5}V_9$) was mostly BCC.

The XRD pattern comparison shown in Fig. 8 demonstrates that a significant amount of a second, ordered phase is prevalent in the sample composition with a high predicted ODTT of 1408 and 1628 K. In contrast, the sample with a low ODTT (489 K) was predominantly a single BCC phase. Although more experiments and samples could further detail the accuracy of the calculations, the methodology certainly indicates a consistency between the calculations and experimental observations. Hence, this demonstrates the use of the ODTT as a design parameter to inform experiments on compositions with high or low propensity to phase decompose at the temperatures of interest.

4.3 ODTT calculation details

The calculations of the ODTT in this study consider both H_{mix} and SRO parameters. The need for the cross validation arises from the fact that sometimes the second derivative of H_{mix} produces several inflection points due to noise in the data and becomes hard to just select one temperature as the ODTT. As for the SRO, a cutoff must be defined which adds uncertainty. Combining insight from both parameters results in the most accurate approach.

The ODTTs of WTa binary alloys in our simulations are about 300 K, which is significantly lower compared to phase diagrams reported in the literature, with transition temperatures between B2 and A2 phases above 500 K [62]. The reason for this discrepancy is that, at low temperatures, WTa binary alloys exhibit numerous competing phases, such as $W_{15}Ta$, W_7Ta, W_4Ta, W_2Ta, W_5Ta_3, W_6Ta_6, W_5Ta_7, W_4Ta_9 and W_4Ta_{12}, with the ODTTs of these phases ranging from 140 to 600 K [63]. The most dominant phases are W_2Ta, W_5Ta_3 and W_6Ta_6 which have comparably low H_{mix} at 0 K, around -0.11 eV/atom. The ODTTs of these three phases range from 550 to 600 K [63]. As an example, the configurations of WTa equiatomic alloy at 200 and 400 K are shown in Figure 9 (a). At 200 K, we can clearly observe intermetallic phases while at 400 K, there are some clustered domains, but it is difficult to definitively identify them as ordered phases. Since different intermetallic phases are significantly different in the first nearest neighbor (1NN) and second nearest neighbor (2NN) arrangements, we have plotted the WTa 1NN and 2NN SRO parameters in Figure 9 (b). The SRO parameters are relatively small (from -0.5 to 0.3) and decrease rapidly in magnitude from around 270 K. Furthermore, H_{mix} does not show any inflection point for temperatures higher than 270 K (Figure 9 (c)). It is important to note that in this study, even at temperatures higher than the ODTT, clustering is still present, though their fraction is smaller than that of the disordered regions.

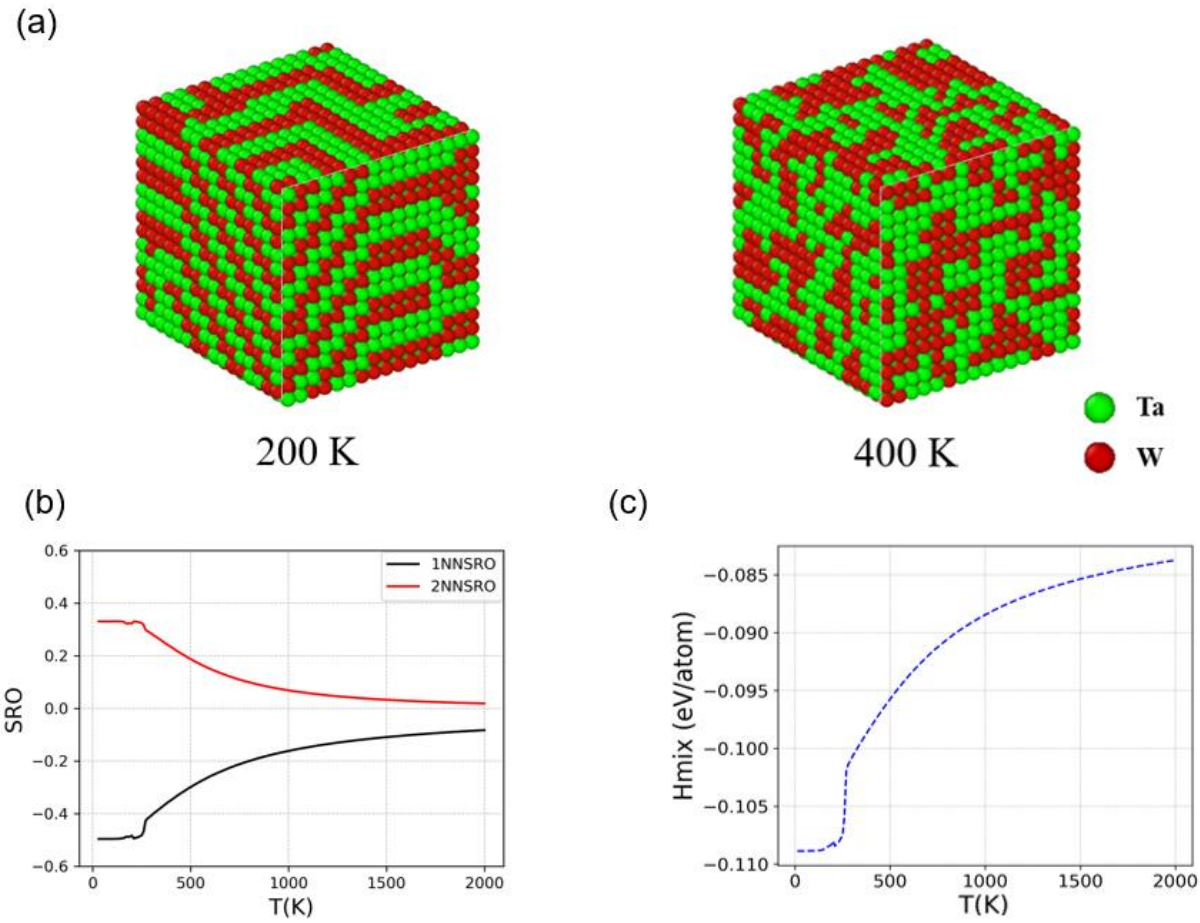

Figure 9. Configuration and SRO of WTa equiatomic alloy

4.4 Limitations on the fitting of thermodynamic databases from cluster expansion results

Since the Monte Carlo calculations aim to find the atomic structure with the lowest Gibbs free energy, a composition located between two minima of the Gibbs free energy will undergo phase decomposition, resulting in a decrease of the free energy and leading to the formation of a miscibility gap, i.e., a straight line in the Gibbs free energy. However, the CALPHAD model predicts the free energy of mixing as a polynomial of high order in the composition. This has proven accurate for solid solution phases, but it will not reproduce the alloy free energy inside a miscibility gap, as it is given by the CE, which is the equilibrium free energy. Instead of fitting with the CE data in the whole composition range, OpenCALPHAD needs the free energy of each phase, i.e., solid solutions and intermetallic compounds if present. This fact complicates the calculation of phase diagrams at low temperatures based on CE data, accounting for all phases, as it would imply the knowledge of such phases *a priori*. To overcome this challenge, we tried to use the ground state structures predicted by ATAT as the intermetallic compounds, but comparing with the results from the Monte Carlo simulations we could not always identify the same structures. This implies that one would need to run CE-MC for different compositions to identify stable compounds, compute the enthalpy of mixing of those and add to the potential phases including solid solutions. Once we have all potential phases, we would need to perform a common

tangent construction with all of them to obtain the solubility limits, which we have decided to leave for a necessary future work. Because of this issue, we focus on the generation of phase diagrams at high temperature (2000 K) where the probability of having only solid solution phases is high. Furthermore, CE contains a term on the interfacial free energy that is not included in the thermodynamic limit described in the CALPHAD approach, which will lead to deviations in the comparison of free energies. This issue is still present in the CrW binary system. In the atomic structures shown in Figure 10 (a), we can observe some clustering from 20% Cr to 80% Cr compositions at 2000 K. The CrW first and second nearest neighbor SRO parameters of $Cr_{40}W_{60}$ composition in Figure 10 (b) are consistent with this conclusion since they are slightly positive (characteristic of repulsive interaction between Cr and W) and keep going down to 0 as temperature increases. More importantly, Figure 10 (c) illustrates the G_{mix} of CrW binary alloys. The blue dots denote the results of the G_{mix} from CE, showing two local minima at 20% Cr and 80% Cr, highlighting the presence of a miscibility gap between those compositions. Inside this gap, G_{mix} as predicted by CE should be a straight line since, as explained above, the MC drives the system to equilibrium. The red line is a fit to the CE points within the miscibility gap. The difference between the blue dots and the red line can be explained by both errors in the convergence of the Monte Carlo simulations at 2000 K and the interfacial energies mentioned above. To compute the final TDB file, points along the red line were used. OpenCALPHAD then predicts the G_{mix}, shown as green dots, which qualitatively captures the presence of a miscibility gap. However, it fails to quantitatively reproduce the linear behavior within the gap indicated by the red line.

It is worth mentioning that the OpenCALPHAD results were obtained with the model for four elements. Resulting from the common tangent construction, we observe a two-phase region at high Cr concentration (see Fig. 7), which should be single phase according to the G_{mix} shown in Fig. 10 (c). To clarify the origin of this discrepancy, we have fitted a TDB file just for the WCr binary and computed G_{mix} and the number of phases for the whole composition range (see Fig. 11). In this case we observe that the number of phases (Table 2) agrees with the functional form of G_{mix}, which seems to lead to small errors in the calculation of the common tangent from high-order free energy functionals.

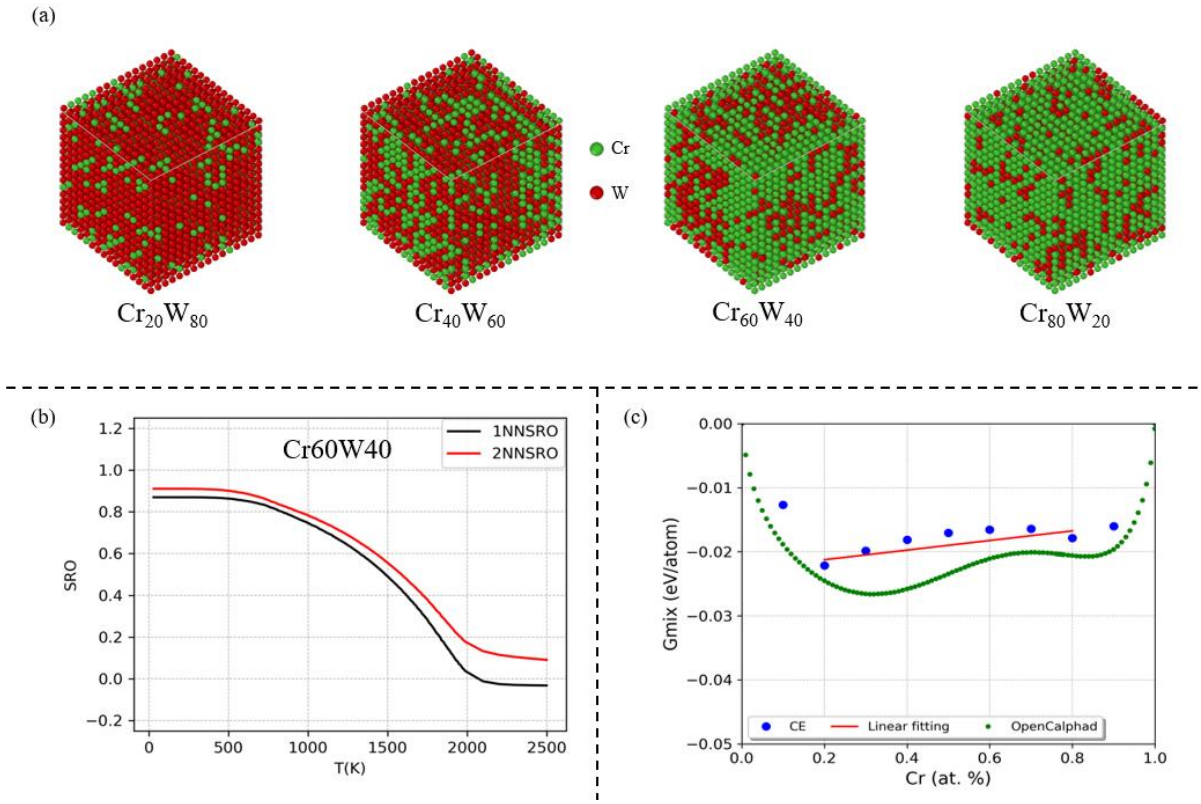

Figure 10. (a) G_{mix} as given by the CE approach and OpenCALPHAD. The red line is a fitting to the CE points highlighting the presence of a miscibility gap. (b) Atomic structure for different compositions of the CrW binary alloy at 2000 K. (c) 1NN and 2NN SRO evolution with temperature of the $Cr_{60}W_{40}$ binary.

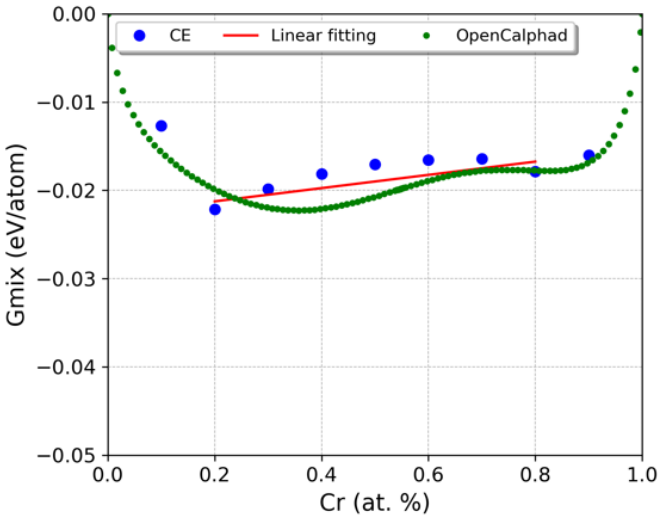

Figure 11. TDB fitting of Cr-W binary alloy

Cr at%	number of phases
10	1
20	1
30	1
40	1
50	2
60	2
70	2
80	2
90	1

Table 2. Phase counts of CrW binary alloy

5. Conclusions

We have calculated the thermodynamic properties of a wide range of CrTaVW HEA compositions using a cluster expansion methodology combined with Monte Carlo sampling and thermodynamic integration. We observe that the entropy of mixing acts as a strong stabilizing factor at high temperatures. For each composition, we have computed the short-range order (SRO) parameters and the order–disorder transition temperatures (ODTT). The ODTT shows strong compositional dependence, ranging from approximately 400 K to 1800 K, with V tending to lower the ODTT and Cr tending to raise it. We demonstrate that ODTT can be used as a design parameter to guide experimental identification of optimal compositions.

In addition, we propose a practical method to construct a phase stability map among competing BCC phases. A thermodynamic database is obtained combining both the cluster expansion (CE) and CALPHAD, enabling equilibrium phase prediction across the composition space by using the common tangent method. This work contributes to the development of an experimentally-validated computational framework to accelerate HEA design based on thermodynamic modeling.

.

Data availability

Data will be made available on request.

Acknowledgments

Funding from the U.S. Department of Energy, Advanced Research Projects Agency-Energy under contract DE-AR0001541 is gratefully acknowledged.
Additionally, this material is based on work supported by the National Science Foundation under Grant Nos. MRI 2024205, MRI 1725573, and CRI 2010270 for allotment of compute time on the Clemson University Palmetto Cluster.

References

[1] Suzuki, S., Ueda, Y., Tokunaga, K., Sato, K., & Akiba, M. (2003). Present research status on divertor and plasma facing components for fusion power plants. Fusion science and technology, 44(1), 41-48.

[2] Ueda, Y., Coenen, J. W., De Temmerman, G., Doerner, R. P., Linke, J., Philipps, V., & Tsitrone, E. (2014). Research status and issues of tungsten plasma facing materials for ITER and beyond. Fusion engineering and design, 89(7-8), 901-906.

[3] Abernethy, R. G. "Predicting the performance of tungsten in a fusion environment: a literature review." Materials Science and Technology 33.4 (2017): 388-399.

[4] Takamura, S., Ohno, N., Nishijima, D., & Kajita, S. (2006). Formation of nanostructured tungsten with arborescent shape due to helium plasma irradiation. Plasma and fusion research, 1, 051-051.

[5] Nishijima, D., Ye, M. Y., Ohno, N., & Takamura, S. (2003). Incident ion energy dependence of bubble formation on tungsten surface with low energy and high flux helium plasma irradiation. Journal of nuclear materials, 313, 97-101.

[6] Miyamoto, M., Mikami, S., Nagashima, H., Iijima, N., Nishijima, D., Doerner, R. P., ... & Sagara, A. (2015). Systematic investigation of the formation behavior of helium bubbles in tungsten. Journal of Nuclear Materials, 463, 333-336.

[7] Miyamoto, M., Mikami, S., Nagashima, H., Iijima, N., Nishijima, D., Doerner, R. P., ... & Sagara, A. (2015). Systematic investigation of the formation behavior of helium bubbles in tungsten. Journal of Nuclear Materials, 463, 333-336.

[8] Yeh, J. W., Chen, S. K., Lin, S. J., Gan, J. Y., Chin, T. S., Shun, T. T., ... & Chang, S. Y. (2004). Nanostructured high‐entropy alloys with multiple principal elements: novel alloy design concepts and outcomes. Advanced engineering materials, 6(5), 299-303.

[9] George, E. P., Raabe, D., & Ritchie, R. O. (2019). High-entropy alloys. Nature reviews materials, 4(8), 515-534.

[10] Miracle, D. B., & Senkov, O. N. (2017). A critical review of high entropy alloys and related

concepts. Acta Materialia, 122, 448-511.

[11] Li, Y., Sun, Y., Cheng, L., Yuan, Y., Jia, B., He, J., ... & Zhu, Q. (2022). Preliminary exploration of a WTaVTiCr high-entropy alloy as a plasma-facing material. Nuclear Fusion, 62(12), 126002.

[12] G. Pu et al., “A comparative study of irradiation response in amorphous TaTiWVCr refractory high entropy alloy with the counterpart of tungsten films,” Intermetallics (Barking), vol. 156, p. 107850, May 2023, doi: 10.1016/J.INTERMET.2023.107850.

[13] Chen, Wei-Ying, et al. "Irradiation effects in high entropy alloys and 316H stainless steel at 300 C." Journal of Nuclear Materials 510 (2018): 421-430.

[14] Yang, Lixin, et al. "High He-ion irradiation resistance of CrMnFeCoNi high-entropy alloy revealed by comparison study with Ni and 304SS." Journal of Materials Science & Technology 35.3 (2019): 300-305.

[15] He, Mo-Rigen, et al. "Mechanisms of radiation-induced segregation in CrFeCoNi-based single-phase concentrated solid solution alloys." Acta Materialia 126 (2017): 182-193.

[16] Shen, Shangkun, et al. "Irradiation damage and swelling of carbon-doped Fe38Mn40Ni11Al4Cr7 high-entropy alloys under heavy ion irradiation at elevated temperature." Journal of Materials Science 55 (2020): 17218-17231.

[17] Chang, Stanley, et al. "Irradiation-induced swelling and hardening in HfNbTaTiZr refractory high-entropy alloy." Materials letters 272 (2020): 127832.

[18] Xia, S. Q., et al. "Irradiation resistance in AlxCoCrFeNi high entropy alloys." Jom 67 (2015): 2340-2344.

[19] Yang, Tai-ni, et al. "Influence of irradiation temperature on void swelling in NiCoFeCrMn and NiCoFeCrPd." Scripta Materialia 158 (2019): 57-61.

[20] Bradbury, N. E., et al. "The Scattering and Absorption Cross Section of Neutrons in Cobalt." Physical Review 52.10 (1937): 1023.

[21] Ustrzycka, A., F. J. Dominguez-Gutierrez, and W. Chromiński. "Atomistic analysis of the mechanisms underlying irradiation-hardening in Fe-Ni-Cr alloys." International Journal of Plasticity (2024): 104118.

[22] Voyevodin, V. N., et al. "Effect of irradiation on microstructure and hardening of Cr–Fe–Ni–Mn high-entropy alloy and its strengthened version." Philosophical Magazine 100.7 (2020): 822-836.

[23] Raman, S., et al. "Thermal-neutron capture by Ni 58, Ni 59, and Ni 60." Physical Review C—Nuclear Physics 70.4 (2004): 044318.

[24] Luneville, Laurence, Jean Christphe Sublet, and David Simeone. "Impact of nuclear transmutations

on the primary damage production: The example of Ni based steels." Journal of Nuclear Materials 505 (2018): 262-266.

[25] Şimşek, Telem, et al. "FeCoNiMnCr high-entropy alloys (HEAs): Synthesis, structural, magnetic and nuclear radiation absorption properties." Ceramics International 49.15 (2023): 25364-25370.

[26] Xue, Juanqin, et al. "Selective laser melting additive manufacturing of tungsten with niobium alloying: microstructure and suppression mechanism of microcracks." Journal of Alloys and Compounds 874 (2021): 159879.

[27] M. Moorehead et al., "High-throughput synthesis of Mo-Nb-Ta-W high-entropy alloys via additive manufacturing," Mater Des, vol. 187, p. 108358, Feb. 2020, doi: 10.1016/J.MATDES.2019.108358.

[28] Melia, Michael A., et al. "High-throughput additive manufacturing and characterization of refractory high entropy alloys." Applied Materials Today 19 (2020): 100560.

[29] Cheng, Zhaoyi, et al. "Irradiation effects in high-entropy alloys and their applications." Journal of Alloys and Compounds 930 (2023): 166768.

[30] Li, Bin, et al. "The study on the magnetic FeCoNiCuAl high-entropy alloy film with excellent corrosion resistance." Vacuum 232 (2025): 113859.

[31] S. San, P. Adhikari, R. Sakidja, J. Brechtl, P.K. Liaw, W.-Y. Ching, Porosity modeling in a TiNbTaZrMo high-entropy alloy for biomedical applications, RSC advances 13(51) (2023) 36468-36476.

[32] Abolkassem, Shimaa, et al. "Microstructure, mechanical, and magnetic properties of powder metallurgy FeCoNiSi–Cu, FeCoNiSi–Mn, and FeCoNiSi-Ti equiatomic HEAs manufactured by spark plasma sintering." Journal of Materials Research and Technology 33 (2024): 9426-9438.

[33] O. El-Atwani, N. Li, M. Li, A. Devaraj, J. Baldwin, M.M. Schneider, D. Sobieraj, J.S. Wróbel, D. Nguyen-Manh, S.A. Maloy, E. Martinez, Outstanding radiation resistance of tungsten-based high-entropy alloys, Science advances 5(3) (2019) eaav2002.

[34] El-Atwani, Osman, et al. "Helium implantation damage resistance in nanocrystalline W-Ta-V-Cr high entropy alloys." Materials Today Energy 19 (2021): 100599.

[35] Warren, B. E. (1990). X-ray Diffraction. Dover. New York, 253.

[36] Cowley, J. M. (1950). An approximate theory of order in alloys. Physical Review, 77(5), 669.

[37] Sundman, B., Kattner, U. R., Palumbo, M., & Fries, S. G. (2015). OpenCALPHAD-a free thermodynamic software. Integrating Materials and Manufacturing Innovation, 4, 1-15.

[38] Fedorov, Mark, et al. "Composition stability of single fcc phase in Cr–Fe–Mn–Ni alloys: First-principles prediction and experimental validation." Acta Materialia 255 (2023): 119047.

[39] Wu, Q., He, B., Song, T., Gao, J., & Shi, S. (2016). Cluster expansion method and its application in computational materials science. Computational Materials Science, 125, 243-254.

[40] Seko, A., Koyama, Y., & Tanaka, I. (2009). Cluster expansion method for multicomponent systems based on optimal selection of structures for density-functional theory calculations. Physical Review B, 80(16), 165122.

[41] Nataraj, C., Borda, E. J. L., van de Walle, A., & Samanta, A. (2021). A systematic analysis of phase stability in refractory high entropy alloys utilizing linear and non-linear cluster expansion models. Acta Materialia, 220, 117269.

[42] Newman, Mark EJ, and Gerard T. Barkema. Monte Carlo methods in statistical physics. Clarendon Press, 1999.

[43] Nicholas Metropolis, Arianna W. Rosenbluth, Marshall N. Rosenbluth, Augusta H. Teller, Edward Teller; Equation of State Calculations by Fast Computing Machines. J. Chem. Phys. 1 June 1953; 21 (6): 1087–1092.

[44] Van De Walle, Axel, M. Asta, and G. Ceder. "The alloy theoretic automated toolkit: A user guide." CALPHAD 26.4 (2002): 539-553.

[45] Van De Walle, A. (2009). Multicomponent multisublattice alloys, nonconfigurational entropy and other additions to the Alloy Theoretic Automated Toolkit. CALPHAD, 33(2), 266-278.

[46] Sanchez, J. M., Francois Ducastelle, and Denis Gratias. "Generalized cluster description of multicomponent systems." Physica A: Statistical Mechanics and its Applications 128.1-2 (1984): 334-350.

[47] Sanchez, J. M. "Foundations and practical implementations of the cluster expansion." Journal of Phase Equilibria and Diffusion 38.3 (2017): 238-251.

[48] Chinnappan, Ravi, B. K. Panigrahi, and Axel van de Walle. "First-principles study of phase equilibrium in Ti–V, Ti–Nb, and Ti–Ta alloys." CALPHAD 54 (2016): 125-133.

[49] Ducastelle, F. R. A. N. C. O. I. S. "Order and phase stability in alloys." Interatomic Potential and Structural Stability. Springer, Berlin, Heidelberg, 1993. 133-142.

[50] Fernández-Caballero, Antonio, et al. "Short-range order in high entropy alloys: theoretical formulation and application to Mo-Nb-Ta-VW system." Journal of Phase Equilibria and Diffusion 38 (2017): 391-403.

[51] Connolly, J. W. D., and A. R. Williams. "Density-functional theory applied to phase transformations in transition-metal alloys." Physical Review B 27.8 (1983): 5169.

[52] Andrew M. Alvarado, Chanho Lee, Jan S. Wróbel, Damian Sobieraj, Duc Nguyen-Manh, Jonathan D. Poplawsky, Saryu Jindal Fensin, Enrique Martinez, Osman El-Atwani, Predicting short-range order

evolution in WTaCrVHf refractory high-entropy alloys, Scripta Materialia, Volume 233, 2023, 115506.

[53] Sobieraj, Damian, et al. "Chemical short-range order in derivative Cr–Ta–Ti–V–W high entropy alloys from the first-principles thermodynamic study." Physical Chemistry Chemical Physics 22.41 (2020): 23929-23951.

[54] Mirebeau, I., M. Hennion, and G. Parette. "First measurement of short-range-order inversion as a function of concentration in a transition alloy." Physical Review Letters 53.7 (1984): 687.

[55] Stukowski, A. (2009). Visualization and analysis of atomistic simulation data with OVITO–the Open Visualization Tool. Modelling and simulation in materials science and engineering, 18(1), 015012.

[56] Fu, Xiaoyu, et al. "Phase stability and transition of CrTaVW high-entropy alloy." Journal of Alloys and Compounds 1002 (2024): 175481.

[57] Van de Walle, A., Sun, R., Hong, Q. J., & Kadkhodaei, S. (2017). Software tools for high-throughput CALPHAD from first-principles data. CALPHAD, 58, 70-81.

[58] Chen, Chi-San, et al. "Novel cermet material of WC/multi-element alloy." International Journal of Refractory Metals and Hard Materials 43 (2014): 200-204.

[59] Lin, Chun-Ming, et al. "New TiC/Co 1.5 CrFeNi 1.5 Ti 0.5 cermet with slow TiC coarsening during sintering." Jom 66 (2014): 2050-2056.

[60] Gao, Michael C., et al., eds. High-entropy alloys: fundamentals and applications. Springer, 2016.

[61] Klein, Sanford, and Gregory Nellis. Thermodynamics. Cambridge University Press, 2011.

[62] Turchi, Patrice EA, et al. "Interface between quantum-mechanical-based approaches, experiments, and CALPHAD methodology." CALPHAD 31.1 (2007): 4-27.

[63] Muzyk, M., et al. "Phase stability, point defects, and elastic properties of WV and WTa alloys." Physical Review B—Condensed Matter and Materials Physics 84.10 (2011): 104115.